Title	Solution phase growth and analysis of super-thin zigzag tin selenide nanoribbons
Author(s)	Davitt, Fionán; Rahme, Kamil; Raha, Sreyan; Garvey, Shane; Roldan-Gutierrez, Manuel; Singha, Achintya; Chang, Shery L. Y.; Biswas, Subhajit; Holmes, Justin D.
Publication date	2022-01-05
Original citation	Davitt, F., Rahme, K., Raha, S., Garvey, S., Roldan-Gutierrez, M., Singha, A., Chang, S. L. Y., Biswas, S. and Holmes, J. D. (2022) 'Solution phase growth and analysis of super-thin zigzag tin selenide nanoribbons', Nanotechnology, 33(13), 135601(12pp). doi: 10.1088/1361-6528/ac4354
Type of publication	Article (peer-reviewed)
Link to publisher's version	http://dx.doi.org/10.1088/1361-6528/ac4354 Access to the full text of the published version may require a subscription.
Rights	© 2022, the Authors. Published by IOP Publishing Ltd. Original content from this work may be used under the terms of the Creative Commons Attribution 4.0 licence. Any further distribution of this work must maintain attribution to the author(s) and the title of the work, journal citation and DOI. https://creativecommons.org/licenses/by/4.0/
Item downloaded from	http://hdl.handle.net/10468/12998

University College Cork, Ireland
Coláiste na hOllscoile Corcaigh

PAPER • OPEN ACCESS

Solution phase growth and analysis of super-thin zigzag tin selenide nanoribbons

To cite this article: Fionán Davitt *et al* 2022 *Nanotechnology* **33** 135601

View the article online for updates and enhancements.

Solution phase growth and analysis of super-thin zigzag tin selenide nanoribbons

Fionán Davitt[1], **Kamil Rahme**[1,2], **Sreyan Raha**[3], **Shane Garvey**[1],
Manuel Roldan-Gutierrez[4], **Achintya Singha**[3] , **Shery L Y Chang**[4,5],
Subhajit Biswas[1,*] and **Justin D Holmes**[1]

[1] School of Chemistry & AMBER Centre, University College Cork, Cork, T12 YN60, Ireland
[2] Department of Sciences, Faculty of Natural and Applied Science, Notre Dame University (Louaize), Zouk Mosbeh 1200, Lebanon
[3] Department of Physics, Bose Institute, Kolkata, India
[4] Eyring Materials Center and School of Molecular Sciences, Arizona State University, Tempe, AZ 85287, United States of America
[5] Electron Microscopy Unit, Mark Wainwright Analytical Centre and School of Materials Science and Engineering, University of New South Wales, Sydney, NSW 2052, Australia

E-mail: s.biswas@ucc.ie

CrossMark

Abstract

Tin selenide (SnSe), a highly promising layered material, has been garnering particular interest in recent times due to its significant promise for future energy devices. Herein we report a simple solution-phase approach for growing highly crystalline layered SnSe nanoribbons. Polyvinylpyrrolidone (PVP) was used as a templating agent to selectively passivates the (100) and (001) facets of the SnSe nanoribbons resulting in the unique growth of nanoribbons along their b-axis with a defined zigzag edge state along the sidewalls. The SnSe nanoribbons are few layers thick ($\sim$20 layers), with mean widths of $\sim$40 nm, and achievable length of $>$1 μm. Nanoribbons could be produced in relatively high quantities ($>$150 mg) in a single batch experiment. The PVP coating also offers some resistance to oxidation, with the removal of the PVP seen to lead to the formation of a $SnSe/SnO_x$ core-shell structure. The use of non-toxic PVP to replace toxic amines that are typically employed for other 1D forms of SnSe is a significant advantage for sustainable and environmentally friendly applications. Heat transport properties of the SnSe nanoribbons, derived from power-dependent Raman spectroscopy, demonstrate the potential of SnSe nanoribbons as thermoelectric material.

Supplementary material for this article is available online

Keywords: nanoribbon, tin selenide, Raman spectroscopy, 1d van-der Waals structure

(Some figures may appear in colour only in the online journal)

Introduction

Quasi-one-dimensional (1D) nanoribbon structures, formed from two-dimensional (2D) layered materials, have exciting and unique physical properties compared to their conventional 2D, or bulk counterparts. Engineering nanostructures into these confined nanoribbon morphologies, where length > width > thickness, is especially relevant for layered materials due to the added advantage of shape and size-dependent optical and

electronic properties that are achievable in such forms. These include the ability to tailor the bandgap, charge carrier effective mass, electrical polarization and phonon transport in the material [1–8]. Layered materials are formed from tightly bound atomic 2D planes, which are then separated by weakly bound Van der Waals bonds along one crystal axis. 2D layered materials have been widely studied, with exciting novel properties achievable through manipulation and exfoliation of the material layers [9]. Confining 2D layers into nanoribbon morphology will provide the added advantages of a 1D pathway for charge carriers, compatibility with the new-age transistor fabrication processes (Fin-field effect transistors (FETs), gate-all-around FET, etc), and ease of realizing channel doping in a FET device.

Group IV–VI monochalcogenide materials have shown great promise for electronic, optoelectronic and energy device applications, [10, 11] with research into these areas being a rapidly growing field of research. Among group IV–VI monochalcogenides, SnSe is a highly versatile metal chalcogenide material with applications in electronic [12, 13], optoelectronic [14, 15], memory [12], and also high potential in a wide spectrum of energy technologies, e.g. thermoelectric devices [16] and solar cells for energy harvesting [17, 18], as well as an anode material for Li-ion batteries for energy storage [19–21]. At room temperature, SnSe crystallises in an orthorhombic Pnma 62 structure, which is a highly anisotropic structure with different lattice constants along each crystal axis. Notably, SnSe forms in a layered crystal structure, with tightly bound bonds along the *b* and *c* axis and relatively weak van der Waals bonding along the *a* axis (see supplementary information figure S1 (available online at stacks.iop.org/NANO/33/135601/mmedia) for a schematic of the SnSe crystal structure). Additionally, it has been shown that the anisotropic nature of SnSe results in noticeable differences in the physical properties, such as a very high thermoelectric figure of merit ($ZT = 2.62$) along the *b*-axis for bulk SnSe [22]. This anisotropic nature shows that the ability to selectively tailor the orientation and termination of the SnSe crystals (e.g. in nanoribbons) would be of significant value to this research field.

Other group IV chalcogenides such as SnS has been explored in nanoribbon forms [23, 24]. Very recently SnSe nanoribbons of ∼10 nm thickness were also achieved on mica substrate via vapour phase deposition at high thermal budget [25]. However, simplistic, high yield solution-phase growth of free standing SnSe nanoribbons currently remains experimentally elusive, and is key for implementation of this material in functional devices such as in thermoelectric generators. Theoretical calculations predicted the immense potential of SnSe nanoribbons in semiconducting and thermoelectric devices. Armchair SnSe nanoribbons are predicted to be semiconducting in nature [26]. Pristine zigzag SnSe nanoribbons are theorised to be metallic, and will show a metal–semiconductor transition, with an opening of the bandgap if broken bonds are present [27]. A relatively high Seebeck coefficient ($\approx 1720\ \mu V\ K^{-1}$) and low thermal conductivity have also been calculated for SnSe nanoribbons with a very low width [26]. A combination of crystal engineering coupled with a nanoribbon morphology thus provides great

potential for further manipulating the physical properties of SnSe, which is not attainable with other morphological features. To this end, new and easy to implement synthetic methods for the growth and morphological engineering of SnSe nanoribbons are required.

Many solution-based methods exist for the synthesis of metal chalcogenide materials, with advantages lying in the ease and scalability of these methods versus costly vapour deposition based methods. Though other SnSe nanostructures such as nanoparticles, [28] nanorods, [29] large nanobelts [30] and 2D like flakes [31, 32] have previously been synthesised in solution using directing and capping agents such as oleylamine, ethanolamine and 1,10-phenanthroline, growth of SnSe nanoribbons is still elusive in any solution phase processing. Additionally, developing a green synthesis method for the high yield and controllable synthesis of these materials is of paramount importance if they are to be successfully incorporated into future electronic and energy devices. Polyvinylpyrrolidone (PVP) is an alternative nontoxic and bio-compatible surface capping and structure-directing agent, that is commonly used for the controlled synthesis of nanoparticles [33] and nanowires, [34] due to its non-toxic nature [35]. PVP is known to offer selective shape control in solution grown crystalline materials, offering the tailored growth of nanowire structures by selective binding to different crystal planes [36]. To the best of our knowledge, PVP has never been used as a templating agent to grow SnSe or other group IV monochalcogenides in 1D nanoform. PVP has been shown to demonstrate biocompatibility in combination with SnSe, [37] where it was used to surface passivate SnSe nanorods in a post-growth treatment. However, passivation of SnSe with PVP during growth was not studied previously.

While SnSe nanowires have been previously explored, through both chemical vapour deposition [12, 38, 39] and solution based methods [40, 41], herein we report for the first time, the simple, environment-friendly and scalable solution phase synthesis of super-thin (∼20 layers thick) SnSe nanoribbons. The nanoribbons are single crystalline throughout and are synthesised using a simple and scalable approach with readily available precursor compounds and PVP as a templating agent. SnSe nanoribbons were structurally analysed in detail via high-resolution transmission electron microscopy. SnSe nanoribbons have a zigzag structure with a ⟨010⟩ growth direction (along *b*-axis), which is highly relevant for thermoelectric applications. A laser-induced heat generation and heat transport study for nanoribbons during Raman measurements, by analysing the Raman peak position, portray SnSe nanoribbons as a promising thermoelectric material.

Experimental

SeO$_2$ (99.8%), polyvinylpyrrolidone (PVP, average molecular weight = 40 000 kDa), KOH, ethylene glycol (emplura), SnCl$_2$.2H$_2$O ($\geqslant$ 99.99%) and ascorbic acid ($\geqslant$ 99%) were all purchased from Sigma Aldrich.

Synthesis of $(Se)_m(PVP)_n$ nanoparticles

SnSe nanoribbons were synthesised by first preparing a solution of $(Se)_m(PVP)_n$ nanoparticle complexes. In a typical synthesis, 0.3327 g of SeO_2 (3 mmol), 3 g PVP and 0.675 g KOH were dissolved in 45 ml of ethylene glycol by heating to 80 °C under Ar while stirring, yielding a very light yellow solution. After complete dissolution the temperature was increased to 195 °C for 18 h, giving a black brown-reddish solution.

Synthesis of SnSe nanoribbons

To synthesise SnSe nanoribbons, two additional solutions were then prepared: (1) 3 mmol $SnCl_2.2H_2O$ (0.675 g) and 0.3 g PVP were dissolved in 12 ml ethylene glycol at 80 °C under stirring and (2) 6 mmol of ascorbic acid (1.0566 g) in 4 ml ethylene glycol was prepared by heating to 80 °C under stirring. These two solutions were then mixed and injected together into the previously prepared solution of Se-PVP nanoparticles in ethylene glycol at 80 °C under stirring. Upon addition of the $SnCl_2$-PVP-ascorbic acid mixture the solution undergoes a colour change to deep red-brownnish ; stirring was maintained for 5 min at 80 °C. This solution was then added to a Teflon lined autoclave (∼7.5 ml per 20 ml cell volume) and heated at 195 °C for between 27 and 76 h. After cooling to room temperature, the solution was washed twice with deionised water followed by centrifugation and then re-dispersed in ethanol.

Characterisation

The synthesised nanomaterials were analysed using a Helios Nanolab 600i scanning electron microscope (SEM). Raman spectroscopy data was taken by a Horiba Jobin Yvon micro-Raman spectrometer, which is equipped with 1800 lines/mm grating and a peltier cooled CCD. An Ar^+ laser of wavelength 488 nm was used to excite the sample and a $50\times$ objective was used to focus the laser on sample as well as to collect the data in backscattering geometry. The crystal structure of the product was confirmed by x-ray diffraction (XRD) using a Philips X'pert Pro MPD equipped with a Panalytical Empyrean Cu x-ray tube and a Philips X'celerator detector. X-ray photoelectron spectroscopy (XPS) analysis was undertaken on an Oxford Applied Research Escabase XPS system with a base pressure of 5×10^{-10} mbar and a non-monochromated Al Kα x-ray source at 200 W. Survey spectra were recorded between 0 and 1000 eV at a step size of 0.7 eV, a dwell time of 0.3 s and a pass energy of 100 eV. Core levels scans were acquired at a step size of 0.1 eV, a dwell time of 0.1 s and a pass energy of 20 eV. CasaXPS software was used for spectra processing with peaks corrected to a Shirley background and fitted to Voigt profiles. Charge correction was applied to the C 1s peak at 285 eV. Samples were drop-cast onto a carbon coated TEM grid for detailed microscopy analysis. TEM analysis was performed on a JEOL 2100 electron microscope operating at 200 kV. EDX elemental mapping was performed at 30 kV on a Helios Nanolab 600i. High annular dark field and bright field STEM imaging and electron energy loss spectroscopy (EELS) was performed on a Probe Corrected JEOL ARM TEM operating at 200 kV. Vesta software was used for the illustration of crystal structures [42].

Results and discussion

SnSe nanoribbons were synthesised through a PVP-mediated solution phase method in a Teflon-lined autoclave (see the experimental section for a detailed procedure). Figure 1 highlights how the morphology of the nanoribbons varies as a function of reaction time at a growth temperature of 195 °C. The product obtained after 27 h of reaction resembles short 1D nanostructures as seen in figure 1(a). EDX analysis revealed these to consist of approximately ∼1:1 Sn:Se (see supplementary information figure S2). The mean lengths and widths of these structures were found to be 216 ± 119 nm and 37 ± 13 nm respectively. A negligible amount of 2D flakes were seen in this reaction. Increasing the reaction time to 50 h resulted in an increase in the mean lengths of the 1D structures but not their widths, i.e. a mean length of 358 ± 185 nm and width of 36 ± 17 nm was obtained. After a 27 h reaction time, 90% of the nanoribbons had lengths < 400 nm, but after 50 h, 62% of the nanoribbons had lengths < 400 nm, with 90% of them below 650 nm; thus indicating that the mean length of the nanoribbons is directly proportional to the reaction time (further statistical analysis is detailed in supplementary information figure S3). Increasing the reaction time from 27 to 50 h therefore resulted in an increase of the mean nanoribbon length by 189 nm. However, the nanoribbon widths remained more or less constant with the increase in the reaction time, with only a negligible increase of ∼1 nm in the mean width being observed for 27 h compared to 50 h reaction. Of note, interestingly, the reactant solution was seen to contain small nanoparticles before transferring to the autoclave for nanoribbon growth (see supplementary information figure S4 for SEM of the drop-casted Se-PVP solution, and figure S5 for the SEM of the dropcasted Se-PVP + $SnCl_2$-PVP mixture). The increase in reaction time thus develops the nanostructures from the initial nanoparticles to 1D nanoribbons, which further increase in length with increasing reaction time. The longest nanoribbons still maintained a mean width similar to the shorter nanoribbons, thus allowing the facile tuning of the aspect ratio with reaction time. Increasing the reaction time to 72 h yielded a further increase in nanoribbon length to 432 ± 191 nm (figures 1(e) + (f)). However, a wider spread in the width values was observed with longer reaction time, corresponding to the presence of a small amount of 2D flakes in the sample. The nanoribbons synthesised after different reaction times were seen to have a similar average thickness of about ∼12 nm. Detail on the nanoribbon thickness will be discussed in the TEM analysis section.

Facilitating the future implementation of SnSe nanoribbons into devices, such as Li-ion batteries and thermoelectric generators, requires production of the nanomaterial in reasonable quantities. Scaling up of 1D SnSe nanorod reactions while
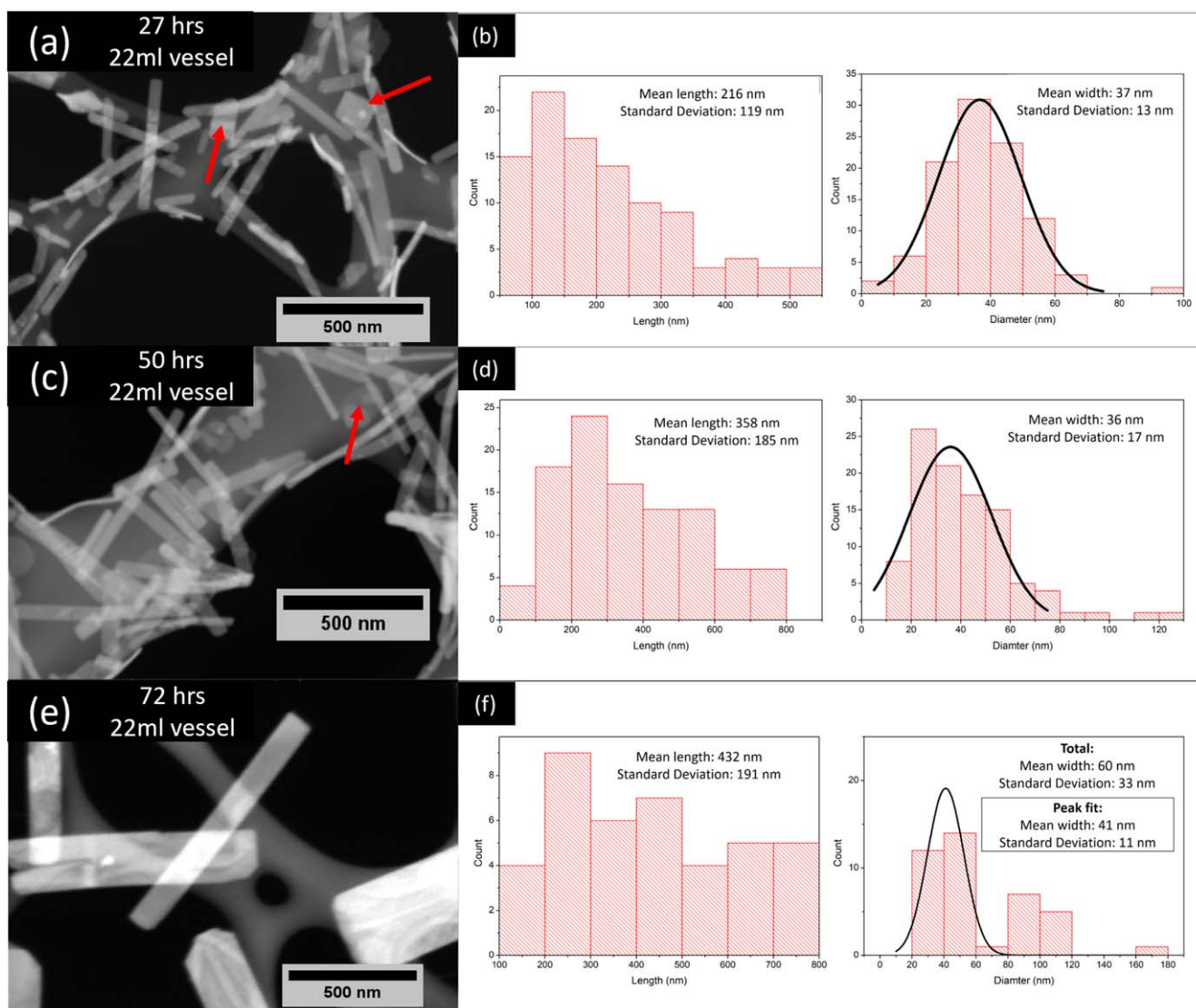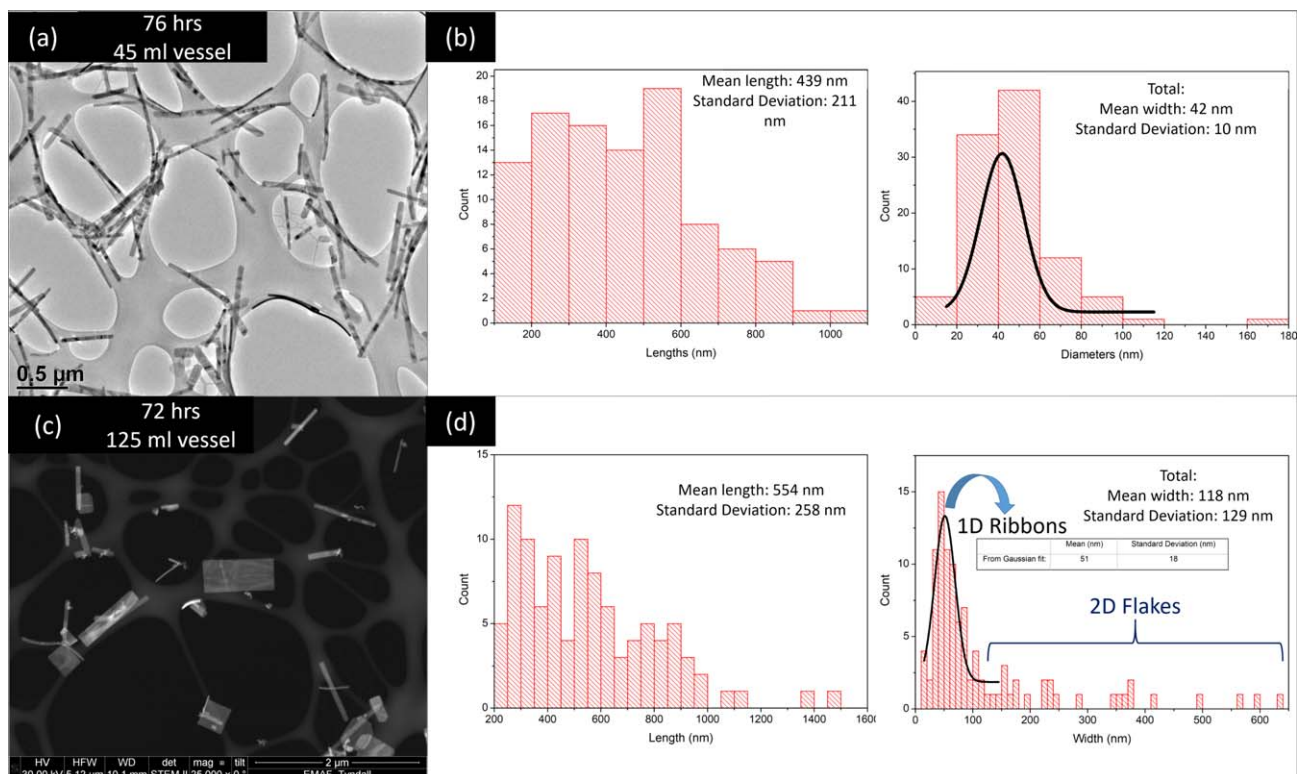
Figure 1. (S)TEM images showing the evolution of the SnSe nanoribbons with respect to the growth conditions: (a) show the structures formed after a reaction time of 27 h, with the statistical analysis of these structures detailed in (b) and (c) shows the effect of increasing the reaction time to 50 h, with the statistical analysis shown in (d). (e) shows an SEM image after a 72 h reaction, with the corresponding statistical analysis in (f). Formation of negligible amount of 2D flakes is shown with red arrows.

maintaining a length: width aspect ratio >5 has previously proved difficult [43]. The batch synthesis of SnSe nanoribbons produced in our approach was found readily scalable, capable of producing hundreds of mg of 1D SnSe nanoribbons with length:width aspect ratios of up to ∼40 achievable (see supplementary information figure S6). To demonstrate the scalability of the growth process, the reaction volume was increased while keeping the reaction temperature and time constant. Figure 2(a) shows the morphology of the structures formed when the reaction volume was roughly doubled to 45 ml vessel, with the reaction temperature kept at 195 °C and the reaction time set at ∼3 d (76 h). The mean length and width of these nanoribbon structures were observed to be 439 ± 211 nm and 42 ± 10 nm respectively, which were consistent with the increase in length with reaction time trend seen for the nanoribbons obtained in smaller 22 ml reaction vessels (figure 1). The nanostructures obtained upon scaling up to a 125 ml reaction vessel at 195 °C for 3 d (72 h) are shown in figure 2(c).

A large amount of SnSe nanostructures (∼158.7 mg) was obtained from the reaction in the 125 ml vessel. At this higher reaction volume a small increase in the ratio of 2D flakes to 1D nanoribbons was observed, giving an 84% yield of nanoribbons to flakes in the 125 ml reaction vessel (see supplementary information figure S6), suggesting that adjustment of the reaction conditions (such as PVP to reactant ratio) may be necessary for higher reaction volumes. Figure 2(d) shows the statistical analysis of the nanostructures obtained in the high volume reaction, revealing a larger spread in the lengths and widths (554 ± 258 nm mean length and 118 ± 129 nm mean width) due to the 2D flakes present in the sample. A small increase in nanostructure length is also observed at the higher reaction volume. After excluding the 2D flakes while analysing the width of the nanoribbon structures, mean width of 51 ± 18 nm was observed for the nanoribbons, relatively similar to that achieved for lower reaction volumes. The aspect ratio of the produced 1D nanoribbons was greatly enhanced

Figure 2. (S)TEM images showing the effect of scaling up the reaction to larger reaction vessels. (a) shows the scaled-up reaction in a 45 ml vessel for 76 h at 195 °C, with (b) detailing the statistical analysis of the nanostructures. (c) Scaled-up reaction in a 125 ml vessel for 72 h at 195 °C. (d) Statistical analysis of the nanostructures produced in the 125 ml vessel. All structures with widths >100 nm were seen to resemble flake-like structures.

through our PVP-assisted approach compared to previously reported solution-grown SnSe nanorods.

Figure 3(a) shows a typical XRD pattern for the SnSe nanoribbons. Phase pure orthorhombic Pnma 62 SnSe was seen, with the 200 and 400 peaks highly prominent. No indication of the presence of any other $SnSe_x$ phases such as $SnSe_2$ was seen in the XRD, proving the high phase purity of the SnSe nanoribbons synthesised. Figure 3(b) shows a Raman spectrum taken from a sample of the SnSe nanoribbons (after 76 h in the 45 ml vessel). Clear peaks in the spectrum are seen at 77, 105, 127 and 157 cm^{-1}, which can be assigned to the A_g^1, B_{3g}, A_g^2 and A_g^3 Raman modes of SnSe respectively. At room temperature, bulk SnSe belongs to the Pnma (No. 62) space group (orthorhombic Bravais lattice) and it is expected for Pnma SnSe to possess 12 Raman active modes [44]. Experimental Raman spectra recorded from SnSe nanoribbons depicted four Raman modes (3 A_g and 1 B_{3g}), similar to the ones observed for ultrathin SnSe flakes, SnSe nanolayers and single crystalline SnSe nanosheets [45–47]. However, compared to previously reported Raman analysis for SnSe flakes and 2D layers, different shifts in the Raman modes has been observed. For example, no shift in the B_{3g} Raman mode was observed in comparison with the 25 nm thick SnSe nanosheets, [47] whereas a 3 cm^{-1} red shift and 2 cm^{-1} blue shift in the B_{3g} Raman mode was observed in the SnSe nanoribbon sample compared to previous nanoflake and 2D layered (21 layers) structures, respectively [45, 46]. If we compare the Raman modes from the nanoribbons with the

theoretically predicted Raman modes for bulk SnSe, the A_g^1 and A_g^3 modes are blue shifted by 6 cm^{-1} whereas the A_g^2 and B_{3g} modes are red-shifted by 3 cm^{-1} [44, 48]. The observed Raman shift relative to the bulk and other 2D nanostructures could potentially result from the morphology, shape asymmetry, nanostructure thickness, and anisotropic crystal confinement along the *c*-axis for the SnSe nanoribbons.

Nanoribbons made of few-atom thick lamellar crystals are novel forms of 1D nanomaterials and are ideal systems for investigating the size and dimensionality dependence of fundamental properties. We have also performed a laser power dependent Raman study on a SnSe nanoribbon sample by varying the laser (Ar + 488 nm) power from 0.01 to 0.08 mW to explore the thermophysical properties of the nanoribbon structure. The corresponding Raman spectra of the SnSe nanoribbons with varying laser power are displayed in figure 3(c). To get the peak positions and full width at half maxima, the spectra were fitted with Lorentzian function. It is very clear that the peak positions and peak intensity of all the Raman modes for SnSe nanoribbons change with laser power. The increase in the Raman intensity is due to the increase in photon flux with the laser power. Figure 3(d) shows the variation of peak positions as a function of laser power for the different Raman modes of SnSe nanoribbons. For reference, the same measurement was performed on bulk Si (shown in figure S7 in the supporting information). The peak positions for all the modes associated with SnSe decrease monotonically with increasing laser power, which indicates an
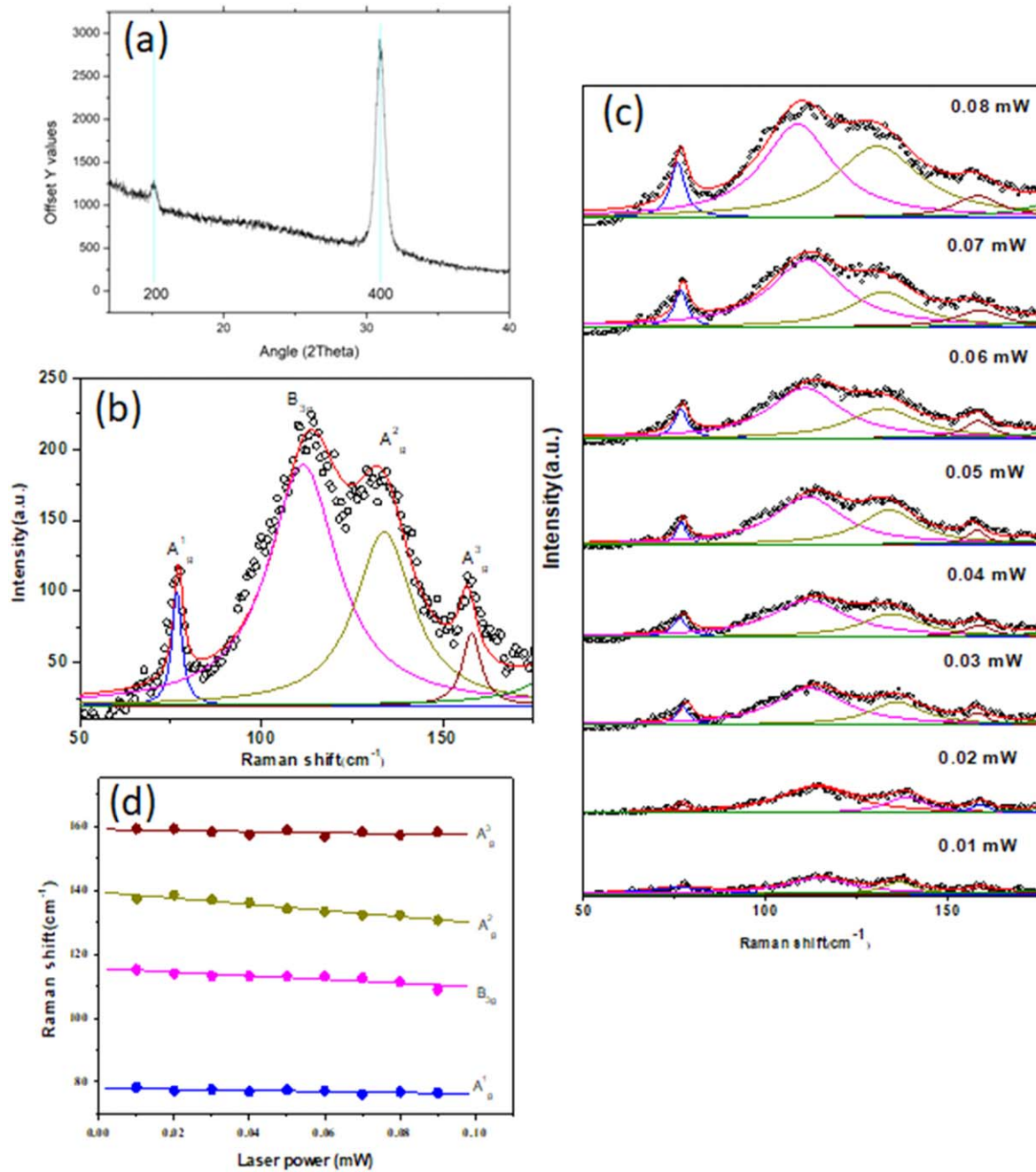
Figure 3. (a) XRD analysis of the SnSe nanoribbons (76 h, 45 ml grown sample). The two strong peaks can be indexed to phase pure orthorhombic Pnma 62 SnSe. (b) Raman analysis of the same sample as in (a). Peaks are clearly seen, corresponding to the A_g^2, B_{3g}, A_g^2 and A_g^3 Raman modes of SnSe respectively (peaks fitted with a Lorentzian function). (c) Laser power dependent Raman spectra for SnSe nanoribbons. (d) Position of different Raman modes of SnSe as a function of laser power. Solid lines are linear fit to the experimental data.

increase in the local temperature of the sample due to laser irradiation [49, 50]. The factors that influence the temperature dependence of Raman shifts and line widths are anharmonic phonon−phonon interaction and thermal expansion. To analyse the red-shift of the Raman modes with laser power we used a linear change in energy: $\omega_P = \omega_o + \chi P$, where P is the laser power, ω_P is the peak position at laser power, P and $\chi = \dfrac{\partial \omega}{\partial P}$ is the measure of the rate of change of peak position with laser power. By fitting the phonon downshift using this equation, the obtained χ values for different SnSe Raman modes vary from 17.5 to 96.4 cm^{-1} mW^{-1} (see table 1 in the supporting information), whereas for the bulk Si χ value is found to be 0.96 cm^{-1} mW^{-1}, which is in agreement with the previous reports [51]. The large red shifts in the SnSe Raman modes with increasing laser power (compared to bulk Si) indicates a high rise in the local temperature for SnSe nanoribbons compared to bulk Si. The high χ value in SnSe compared to Si signifies the slow heat transfer (as thermal conductivity (κ) is inversely proportional to χ [52]) within the SnSe nanoribbon sample because of the low thermal conductivity of the nanoribbons. These results demonstrate the
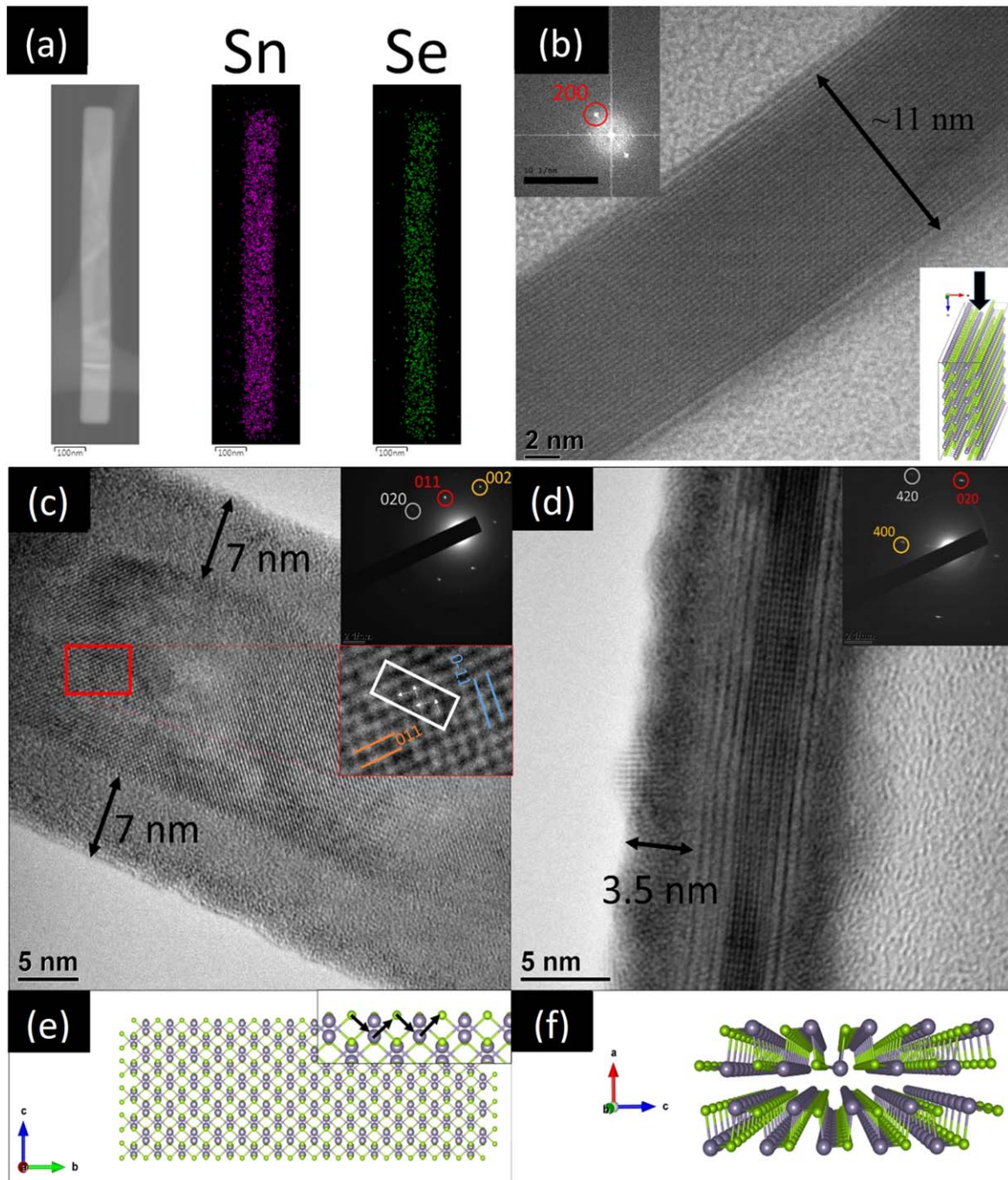
Figure 4. (a) EDX map of a SnSe nanoribbon (72 h, 125 ml grown sample), showing the uniform distribution of Sn and Se throughout the structure. (b) TEM image of a SnSe-PVP nanoribbon (76 h, 45 ml grown sample) oriented close to the [001] zone axis. A nanoribbon thickness of ∼11 nm is observed. The top left inset shows a fast Fourier transform (FFT), with the bottom right inset showing a schematic of the orientation of the nanoribbon (the black arrow indicates the viewing direction of the TEM image). TEM analysis of SnSe nanoribbons: (c) a SnSe nanoribbon oriented along the [100] zone axis, as confirmed from the indexed SAED pattern in the top inset. The bottom inset shows a HRTEM image of a section of the nanoribbon, revealing a zigzag structure of SnSe along the <010> direction. Roughly 7 nm thick amorphous regions can be seen at the edges of the nanoribbon. (d) SnSe nanoribbon oriented along [010] zone axis, as confirmed from the indexed SAED pattern in the inset. Thickness of amorphous regions is ∼ 3.5 nm. (e) SnSe nanoribbon structure viewed down the [100] direction. The zigzag structure is highlighted in the inset. (f) Perspective view of a SnSe nanoribbon cross-section.

potential of SnSe nanoribbons as an efficient thermoelectric material. However, detailed studies of the thermal, electrical and thermoelectric properties of the SnSe nanoribbons are necessary to verify its true potential in thermoelectric devices, which we delegate to a later study.

Figure 4(a) shows an EDX map of a nanoribbon (after 72 h in the 125 ml vessel), revealing the uniform distribution of Sn and Se throughout the nanoribbons, without any elemental segregation. The nanoribbon morphology and thickness were investigated with TEM analysis (figure 4(b)),

however the PVP coating of the nanoribbons presented difficulty with the imaging. A SnSe nanoribbon oriented close to the [001] zone axis is presented in figure 4(b), with a fast Fourier transform (FFT) pattern in the top left inset, indicating the (200) diffraction spot, which is oriented perpendicular to the nanowire growth direction. A thickness of ~11 nm was measured, and as this is along the $\langle 100 \rangle$ direction, this represents the thickness of the nanoribbon. The bottom right inset of figure 4(b) schematically represents how the nanoribbon is oriented in the figure, highlighting how the measured ~11 nm value corresponds to the nanoribbon thickness. A thickness of ~11 nm for the nanoribbon would indicate about 19–20 SnSe layers in the nanoribbon structure. The exact layer number is made difficult to determine by the obscuring effect of the PVP present. In general, thicknesses of between ~11 and 13 nm were observed from the TEM analysis of the SnSe nanoribbons.

In order to facilitate clearer imaging of the crystal structure of the SnSe nanoribbons they were washed in ethanol to remove the majority of the PVP. Figures 4(c) and (d) show TEM images of ethanol washed SnSe nanoribbons grown after 76 h in the 45 ml vessel, with indexed SAED patterns as insets, orientated along the [100] and [001] zone axes, respectively. Another interesting feature of tailored nanoribbon morphologies is the possibility of defined edge states. The nature of the edge states depends not only on the crystal structure of the system, but also on the way they terminate, which influences the physical properties of the nanoribbons. After removing the PVP, the zigzag structure of SnSe along the $\langle 010 \rangle$ direction is clearly seen in the HRTEM image in the inset of figure 4(c). This is of particular interest due to the theoretically predicted semiconductor to metallic transition in very thin Zigzag SnSe nanoribbons [26, 27]. The larger number of morphological variables, such as size, edge-type and thickness, associated with nanoribbon structure over 2D films could allow further scope for better manipulation of their physical properties. After removing the PVP, a dark contrast amorphous layer is also apparent on the surface of the nanoribbons. This amorphous coating is darker in contrast to the previous PVP coating (figure 4(b)) and is shown to consist of SnO_x by EELS analysis (see supplementary information figure S8). SnSe has been shown to oxidise rapidly in air, forming a SnO_x surface of ~6 nm [12, 53], which is consistent with the thickness of the amorphous layer seen in the TEM images; indicating that this layer is formed post-growth, and post removal of the PVP due to atmospheric surface oxidation. The total thickness of the SnSe nanoribbon, visible when it is viewed down the [001] zone axis in figure 4(d), was seen to be ~12 nm, which is also in agreement with the nanoribbon thickness seen when the PVP was present. However, the crystalline core region is reduced to a thickness of ~6 nm, with the rest being formed of amorphous SnO_x. This indicates that the PVP appears to offer some protection to atmospheric oxidation, and removal of the PVP should only be performed directly before the implementation of the SnSe nanoribbons into a device. The SnSe nanoribbons are single crystalline throughout their core, as shown in the HRTEM images and corresponding SAED patterns (figures 4(c) and (d) with SAED patterns in insets). The single crystalline nature of

these SnSe nanoribbons is important to note, as high yield solution phase growth methods can commonly result in the formation of nanomaterials with a polycrystalline or highly defected crystal structure [34, 54]. Growth directions along the $\langle 010 \rangle$ crystal direction of SnSe was observed for every nanoribbon studied (figures 4(c) and (d)), demonstrating a high level of uniformity in the single crystalline nanoribbons. The crystal structure of a $\langle 010 \rangle$ oriented SnSe nanoribbon is illustrated in figures 4(e) and (f). Most previous studies on 1D SnSe nanowires have shown growth directions along either the $\langle 011 \rangle$ or $\langle 100 \rangle$ directions, [12, 39, 41] but in our case, for all nanoribbons analysed, the growth direction was found to be $\langle 010 \rangle$. This growth direction for 1D SnSe has only ever been shown for oleylamine [29] and ethanolamine [30] assisted methods, producing short nanorods and large nanobelts respectively. Growth along the $\langle 010 \rangle$ direction leads to the exposure of energetically unfavourable high energy surface planes for SnSe [55], demonstrating the necessity of a suitable capping agent. In our approach PVP selectively binds to the (100) and (001) SnSe crystal surfaces, facilitating growth along the $\langle 010 \rangle$ direction. Of note, the thermoelectric measurement along the $\langle 010 \rangle$ crystal direction has previously been reported to exhibit an ultralow lattice thermal conductivity and a very high thermoelectric figure of merit for bulk SnSe crystals [22]. Utilising $\langle 010 \rangle$ oriented SnSe nanoribbons for future thermoelectric studies would thus be of significant interest. The potential of the SnSe nanoribbons in thermoelectric is also demonstrated through temperature dependent Raman spectroscopy (figures 3(c) and (d)).

The growth of SnSe in the 1D nanoribbon structure can be explained through the choice of precursors and PVP as surface passivating agent (figure 5). The growth mechanism of such SnSe flakes and nanoribbons is illustrated in figure 5. The growth of SnSe flakes has previously been shown to initiate as a high surface energy (010) and (001) faceted SnSe flake, with the lower surface energy (011) and (0–11) facets forming the surface planes in the later stages of growth (top row-figure 5) [55]. The basal plane of the layered crystal (100) surface possesses the smallest surface energy, resulting in majority of (100) surface in the nanoribbons. For the formation of SnSe nanoribbons, PVP acts to confine the crystal growth in the early (010) and (001) faceted stage and then restricts the growth in other directions by allowing the adatoms addition preferentially along the (010) plane (illustrated in the bottom row of figure 5).

Capping ligands like PVP plays a significant role in inducing directional growth by selectively adsorbing to specific crystal facets and inhibiting the growth of these facets. PVP reduces the surface free energy of a specific type of facet through selective binding or chemisorption. Without any ligand (PVP in our case), the growth of a nanocrystal will proceed along the path that minimizes the total surface free energy of the system. For SnSe, the absence of any capping molecules leads to the formation of nanosheet morphology, as described in the top row of figure 5. However, ascribed to their unique molecular structures and conformations, surface ligands such as PVP can preferentially bind to a certain crystal facet. This mainly depends on the binding energy which is influenced by the symmetry between the molecule
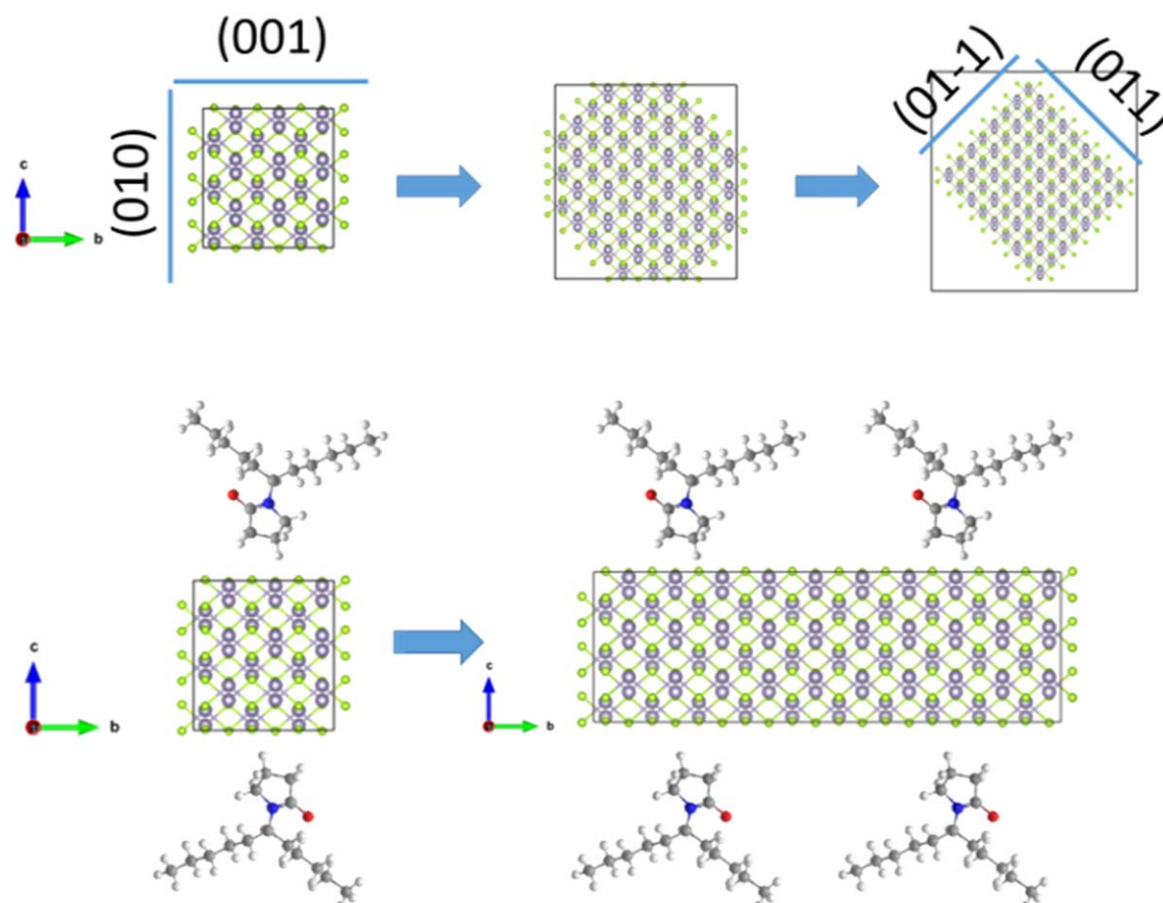
Figure 5. Illustration of the proposed growth of the SnSe nanoribbon crystal structure; at the top is shown the growth mechanism for a 2D SnSe flake, and the bottom shows how PVP leads to the growth of SnSe nanoribbons through the passivation of the (001) facets.

and crystal surface, the surface-sensitive balance between direct bonding and other kinds of attraction (e.g. van der Waals attraction), etc. The role of PVP in surface selective binding and directional growth of metals (e.g. Ag) is well documented. However, a detailed study, incorporating the density functional theory calculations is required for an accurate understanding of the role of PVP in the directional growth of monochalcogenide based nanostructures such as SnSe nanoribbons and nanowires, which is delegated to a future study.

Due to the layered crystal structure of SnSe, crystal growth tends to dominate along the *b* and *c* crystal axes, with minimal growth along the *a*-axis, upon which the SnSe layers are stacked. Thus the use of SeO_2 with a chain structure, and PVP as a passivating agent was crucial for the preferential 1D growth of the layered SnSe structure. The chain structure exhibited by SeO_2 is believed to lead to the formation of a chain $(Se)_m(PVP)_n$ complex, similar to chain $(Se)_m(Oleylamine)_n$ complexes observed in previous 1D SnSe nanowire growth [29]. To these (Se^{2-})-PVP seeds, $SnCl_2.2H_2O$ is then added as a source of Sn^{2+}, which then diffuses into the Se-PVP to form SnSe-PVP nanoparticles (figures S4 and S5 in the supporting information). The SnSe nanoribbons then grow from the SnSe nucleation points, with the aid of PVP as a 1D directing agent. 1D SnSe growth with oleylamine as growth directing reagent at very similar growth temperature ($\sim$175 $^{\circ}$C) resulted in the

formation of nanorod structure [29]. However, much stronger confinement with long-chain PVP polymer resulted in the formation of a much thinner 1D structure in the form of nanoribbons. PVP is a strong capping agent that interacts with the SeO_2 through the strong ionic bonds between the Se^{2-} ions and the amide group oxygen in the PVP chain. Therefore, it is believed that PVP stabilizes the dissolved precursor by amide group steric and electrostatic stabilization and facilitates the growth of nanoribbons. The nanoribbon width and thickness are not seen to increase by any significant amount with increasing length or reaction time, and after the initial nanoribbon formation, the growth continues only by addition along the (010) crystal facets. Additional reaction times lead to further addition along with the (010) crystal facets, and thus longer nanoribbons. The growth of SnSe has commonly been reported to result in the formation of a nanoflake morphology, without the use of any additional surfactants [56].

In a typical growth, SeO_2 was heated in ethylene glycol to reduce the Se^{4+} to Se^{2-} [57], which is important as tin selenides have commonly been reported to form both SnSe and $SnSe_2$ phases, where Sn exists in both 2+ and 4+ oxidation states respectively. The oxidation of Sn^{2+} to Sn^{4+} has previously been shown to be suppressed, during the reaction, by the addition of a surfactant such as L-ascorbic acid, aiding in the formation of phase pure SnSe [58]. The XPS spectrum (Se spectrum) of the ethanol washed SnSe nanoribbon sample
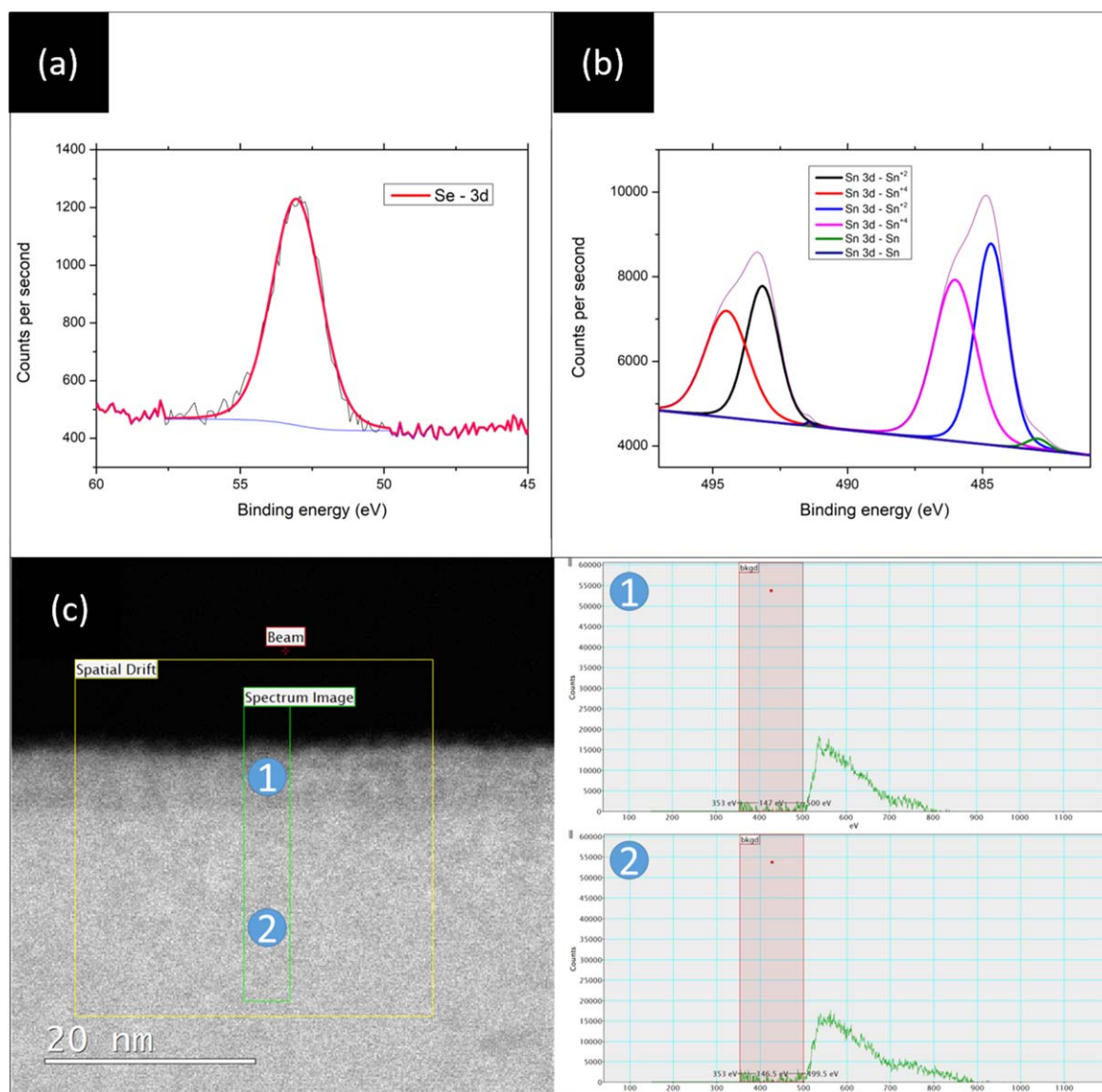
Figure 6. (a) and (b) XPS spectra of Se and Sn binding energies, respectively. (c) EELS analysis of a SnSe nanoribbon: EELS of Sn $M_{4,5}$ Edges and O K edges along a SnSe nanoribbon.

(shown in figure 6(a)) verifies the single oxidation state of Se^{2-}, supporting the high phase purity of the SnSe sample. Though the Sn XPS spectrum (figure 6(b)) reveals three oxidation states for Sn; Sn^0, Sn^{+2} and Sn^{+4}. This is in agreement with the EELS analysis (figure 6(c)), which reveals that the Sn^{4+} results from the surface oxidation of the SnSe nanoribbons, with the body of the nanoribbon remaining single crystalline SnSe. The presence of oxygen at the surface region gives rise to the splitting of EEL spectra at 530–540 eV (figure 6(c)), in contrast to no splitting feature shown in the bulk region of nanoribbon, revealing that the amorphous surface layer (region 1) is composed of SnO_x. SnSe has previously been reported to oxidise rapidly in the air [12, 53]. PVP is expected to offer improved protection from this post-growth oxidation, but oxygen diffusion through the PVP layer will still cause small diameter nanostructures to oxidise gradually over time [59].

Conclusions

The synthesis of few-layer thick single crystalline SnSe nanoribbons has been successfully achieved through a simple solution-based method, using readily available precursors. Non-toxic PVP was used for the first time to direct the 1D growth of SnSe. The easy to scale-up synthesis approach using non-toxic PVP to grow SnSe nanoribbons is ideal for nanoribbons application in biomedical devices, batteries, solar cells, memory devices and thermoelectric generators. SnSe nanoribbons demonstrated high morphological and structural quality, and promising thermophysical properties. The synthesised nanoribbons all grow along the $\langle 010 \rangle$ direction, which has been previously reported to possess a remarkably low lattice thermal conductivity along with this crystal orientation, highlighting the significance of these nanoribbons for potential applications in future thermoelectric devices. The growth along the $\langle 010 \rangle$ direction is uncommon as the crystal

growth along this direction exposes the high surface energy planes in the structure. The uncommon growth along the $\langle 010 \rangle$ direction is achieved for SnSe nanoribbons through the selective binding of PVP to the (100) and (001) surface planes. A better understanding of the nature of the influence of PVP in SnSe systems could lead to future possibilities in material design and non-toxic growth strategies for the solution phase synthesis of SnSe and other group IV monochalcogenides. The growth of very thin $\langle 010 \rangle$ oriented SnSe nanoribbons has not previously been reported, and the successful synthesis of SnSe nanoribbons also enables the future exploration of the previously theorised novel properties of SnSe nanoribbons and other nanoribbon structures, such as a width-dependant tuneable bandgap for application in electronic, energy, and memory devices.

Acknowledgments

Data availability statement

The data that support the findings of this study are available upon reasonable request from the authors.

Conflict of interest

The authors declare no competing financial interest.

ORCID iDs

Achintya Singha https://orcid.org/0000-0001-9930-4087
Subhajit Biswas https://orcid.org/0000-0001-9774-7714

References

[1] Han M Y, Özyilmaz B, Zhang Y and Kim P 2007 Energy band-gap engineering of graphene nanoribbons *Phys. Rev. Lett.* **98** 206805

[2] Xu L C, Song X J, Yang Z, Cao L, Liu R P and Li X Y 2015 Phosphorene nanoribbons: passivation effect on bandgap and effective mass *Appl. Surf. Sci.* **324** 640–4

[3] Cai Y, Zhang G and Zhang Y W 2014 Polarity-reversed robust carrier mobility in monolayer MoS$_2$ nanoribbons *J. Am. Chem. Soc.* **136** 6269–75

[4] Wang H Y, Wang C R, Xu J, Liu X, Xu X F, Xing H Z, Zhao L J and Chen X S 2012 Different temperature dependence of excitonic and defect-related photoluminescence spectra in ZnS nanobelts and nanowires *J. Phys. D: Appl. Phys.* **45** 095301

[5] Fang X S, Ye C H, Zhang L D and Xie T 2005 Twinning-mediated growth of Al$_2$O$_3$ nanobelts and their enhanced dielectric responses *Adv. Mater.* **17** 1661–5

[6] Fang X *et al* 2009 Single-crystalline ZnS nanobelts as ultraviolet-light sensors *Adv. Mater.* **21** 2034–9

[7] Jin X B, Li Y X, Su Y, Guo Z, Gu C P, Huang J R, Meng F L, Huang X J, Li M Q and Liu J H 2016 Porous and single-crystalline ZnO nanobelts: fabrication with annealing precursor nanobelts, and gas-sensing and optoelectronic performance *Nanotechnology* **27** 355702

[8] Tripathi N, Pavelyev V, Sharma P, Kumar S, Rymzhina A and Mishra P 2021 Review of titanium trisulfide (TiS$_3$): a novel material for next generation electronic and optical devices *Mater. Sci. Semicond. Process.* **127** 105699

[9] Nicolosi V, Chhowalla M, Kanatzidis M G, Strano M S and Coleman J N 2013 Liquid exfoliation of layered materials *Science* **340** 1226419–1226419

[10] Gao M R, Xu Y F, Jiang J and Yu S H 2013 Nanostructured metal chalcogenides: Synthesis, modification, and applications in energy conversion and storage devices *Chem. Soc. Rev.* **42** 2986–3017

[11] Zhou X, Zhang Q, Gan L, Li H, Xiong J and Zhai T 2016 Booming development of group IV–VI semiconductors: fresh blood of 2D family *Adv. Sci.* **3** 1600177

[12] Davitt F, Manning H G, Robinson F, Hawken S L, Biswas S, Petkov N, Druenen M, Boland J J, Reid G and Holmes J D 2020 Crystallographically controlled synthesis of SnSe nanowires: potential in resistive memory devices *Adv. Mater. Interfaces* **7** 2000474

[13] Cho S H, Cho K, Park N W, Park S, Koh J H and Lee S K 2017 Multi-layer SnSe nanoflake field-effect transistors with low-resistance Au ohmic contacts *Nanoscale Res. Lett.* **12** 2–7

[14] Pawbake A S, Jadkar S R and Late D J 2016 High performance humidity sensor and photodetector based on SnSe nanorods *Mater. Res. Express* **3** 105038

[15] Zhao S *et al* 2015 Controlled synthesis of single-crystal SnSe nanoplates *Nano Res.* **8** 288–95

[16] Chen Z G, Shi X, Zhao L D and Zou J 2018 High-performance SnSe thermoelectric materials: progress and future challenge *Prog. Mater. Sci.* **97** 283–346

[17] Minnam Reddy V R, Gedi S, Pejjai B and Park C 2016 Perspectives on SnSe-based thin film solar cells: a comprehensive review *J. Mater. Sci., Mater. Electron.* **27** 5491–508

[18] Franzman M A, Schlenker C W, Thompson M E and Brutchey R L 2010 Solution-phase synthesis of SnSe nanocrystals for use in solar cells *J. Am. Chem. Soc.* **132** 4060–1

[19] Wang W, Li P, Zheng H, Liu Q, Lv F, Wu J, Wang H and Guo S 2017 Ultrathin layered SnSe nanoplates for low voltage, high-rate, and long-life Alkali–Ion batteries *Small* **13** 1–7

[20] Cheng Y, Huang J, Li J, Cao L, Xu Z, Luo X, Qi H and Guo P 2019 SnSe/r-GO composite with enhanced pseudocapacitance as a high-performance anode for Li-Ion Batteries *ACS Sustain. Chem. Eng.* **7** 8637–46

[21] Davitt F *et al* 2020 2D SnSe nanonetworks; growth and evaluation for Li-ion battery applications *ACS Appl. Energy Mater.* **3** 6602–10

[22] Zhao L-D, Lo S-H, Zhang Y, Sun H, Tan G, Uher C, Wolverton C, Dravid V P and Kanatzidis M G 2014 Ultralow thermal conductivity and high thermoelectric figure of merit in SnSe crystals *Nature* **508** 373–7

[23] Deng Z, Cao D, He J, Lin S, Lindsay S M and Liu Y 2012 Solution synthesis of ultrathin single-crystalline SnS nanoribbons for photodetectors via phase transition and surface processing *ACS Nano* **6** 6197–207

[24] Lu J, Nan C, Li L, Peng Q and Li Y 2013 Flexible SnS nanobelts: facile synthesis, formation mechanism and application in Li-ion batteries *Nano Res.* **6** 55–64

[25] Liu Z, Ding K, Liu Z, Zhang F, Zeng H, Xu K, Sun Y, Wang D and Li Y 2021 Kinetics-driven one-dimensional

growth of van der waals layered SnSe *J. Phys. Chem.* C **125** 12730–7

[26] Tyagi K, Waters K, Wang G, Gahtori B, Haranath D and Pandey R 2016 Thermoelectric properties of SnSe nanoribbons: a theoretical aspect *Mater. Res. Express* **3** 035013

[27] Huang Y, Ling C, Liu H and Wang S 2014 Edge-, width- and strain-dependent semiconductor-metal transition in SnSe nanoribbons *RSC Adv.* **4** 6933–8

[28] Baumgardner W J, Choi J J, Lim Y-F and Hanrath T 2010 SnSe nanocrystals: synthesis, structure, optical properties, and surface chemistry *J. Am. Chem. Soc.* **132** 9519–21

[29] Wang R, Wei M, Jiang G, Liu W and Zhu C 2014 Study of the preperation of snse nanorods with selenium dioxide as source *Chem. Lett.* **43** 693–5

[30] Guo J, Jian J, Liu J, Cao B, Lei R, Zhang Z, Song B and Zhao H 2017 Synthesis of SnSe nanobelts and the enhanced thermoelectric performance in its hot-pressed bulk composite *Nano Energy* **38** 569–75

[31] Vaughn D D, In S I and Schaak R E 2011 A precursor-limited nanoparticle coalescence pathway for tuning the thickness of laterally-uniform colloidal nanosheets: the case of SnSe *ACS Nano* **5** 8852–60

[32] Li L, Chen Z, Hu Y, Wang X, Zhang T, Chen W and Wang Q 2013 Single-layer single-crystalline SnSe nanosheets *J. Am. Chem. Soc.* **135** 1213–6

[33] Koczkur K M, Mourdikoudis S, Polavarapu L and Skrabalak S E 2015 Polyvinylpyrrolidone (PVP) in nanoparticle synthesis *Dalton Trans.* **44** 17883–905

[34] Jia Y, Ma Y, Lin Y, Tang J and Shi W 2018 Facile synthesis of branched MoS_2 nanowires *Chem. Phys.* **513** 209–12

[35] Jadhav S V, Nikam D S, Khot V M, Thorat N D, Phadatare M R, Ningthoujam R S, Salunkhe A B and Pawar S H 2013 Studies on colloidal stability of PVP-coated LSMO nanoparticles for magnetic fluid hyperthermia *New J. Chem.* **37** 3121–30

[36] Sun Y, Mayers B, Herricks T and Xia Y 2003 Polyol synthesis of uniform silver nanowires: a plausible growth mechanism and the supporting evidence *Nano Lett.* **3** 955–60

[37] Tang Z, Zhao P, Ni D, Liu Y, Zhang M, Wang H, Zhang H, Gao H, Yao Z and Bu W 2018 Pyroelectric nanoplatform for NIR-II-triggered photothermal therapy with simultaneous pyroelectric dynamic therapy *Mater. Horizons* **5** 946–52

[38] Butt F K, Mirza M, Cao C, Idrees F, Tahir M, Safdar M, Ali Z, Tanveer M and Aslam I 2014 Synthesis of mid-infrared SnSe nanowires and their optoelectronic properties *CrystEngComm* **16** 3470

[39] Liu J, Jian J, Yu Z, Zhang Z, Cao B and Du B 2017 Catalyst-free vapor phase growth of ultralong SnSe single-crystalline nanowires *Cryst. Growth Des.* **17** 6163–8

[40] Shen G, Chen D, Jiang X, Tang K, Liu Y and Qian Y 2003 Rapid synthesis of SnSe nanowires via an ethylenediamine-assisted polyol route *Chem. Lett.* **32** 426–7

[41] Liu S, Guo X, Li M, Zhang W H, Liu X and Li C 2011 Solution-phase synthesis and characterization of single-crystalline SnSe nanowires *Angew. Chem.—Int. Ed.* **50** 12050–3

[42] Momma K and Izumi F 2011 VESTA 3 for three-dimensional visualization of crystal, volumetric and morphology data *J. Appl. Crystallogr.* **44** 1272–6

[43] Kundu S, Yi S I and Yu C 2018 Gram-scale solution-based synthesis of SnSe thermoelectric nanomaterials *Appl. Surf. Sci.* **459** 376–84

[44] Chandrasekhar H R, Humphreys R G, Zwick U and Cardona M 1977 Infrared and Raman spectra of the IV-VI compounds SnS and SnSe *Phys. Rev.* B **15** 2177–83

[45] Luo S, Qi X, Yao H, Ren X, Chen Q and Zhong J 2017 Temperature-dependent raman responses of the vapor-deposited tin selenide ultrathin flakes *J. Phys. Chem.* C **121** 4674–9

[46] Ludemann M, Gordan O D, Zahn D R T, Beekman M, Atkins R and Johnson D C 2014 Raman spectroscopy insights into the size-induced structural transformation in snse nanolayers *Langmuir* **30** 8209–14

[47] Jian Z, Zhu H, Wu X, Cui H, Li D, Jiang J, Gao C, Wang Q and Cui Q 2015 Plasma-assisted synthesis and pressure-induced structural transition of single-crystalline SnSe nanosheets *Nanoscale* **7** 10807–16

[48] Liu F *et al* 2018 Phonon anharmonicity in single-crystalline SnSe *Phys. Rev.* B **98** 224309

[49] Majumdar D, Biswas S, Ghoshal T, Holmes J D and Singha A 2015 Probing thermal flux in twinned Ge nanowires through raman spectroscopy *ACS Appl. Mater. Interfaces* **7** 24679–85

[50] Jalilian R, Sumanasekera G U, Chandrasekharan H and Sunkara M K 2006 Phonon confinement and laser heating effects in Germanium nanowires *Phys. Rev.* B **74** 155421

[51] Nikolenko A S 2013 Laser heating effect on Raman spectra of Si nanocrystals embedded into SiOx matrix *Semicond. Phys. Quantum Electron. Optoelectron.* **16** 86–90

[52] Sahoo S, Gaur A P S, Ahmadi M, Guinel M J F and Katiyar R S 2013 Temperature-dependent Raman studies and thermal conductivity of few-layer MoS_2 *J. Phys. Chem.* C **117** 9042–7

[53] Tian H, Wang X F, Mohammad M A, Gou G Y, Wu F, Yang Y and Ren T L 2018 A hardware markov chain algorithm realized in a single device for machine learning *Nat. Commun.* **9** 1–11

[54] Baby B H and Mohan D B 2017 The formation of α-phase SnS nanorods by PVP assisted polyol synthesis: phase stability, micro structure, thermal stability and defects induced energy band transitions *Mater. Chem. Phys.* **192** 317–29

[55] Ma X H, Cho K H and Sung Y M 2014 Growth mechanism of vertically aligned SnSe nanosheets via physical vapour deposition *CrystEngComm* **16** 5080–6

[56] Han G *et al* 2016 Facile surfactant-free synthesis of p-type snse nanoplates with exceptional thermoelectric power factors *Angew. Chem.—Int. Ed.* **55** 6433–7

[57] Skrabalak S E, Wiley B J, Kim M, Formo E V and Xia Y 2008 On the polyol synthesis of silver nanostructures: glycolaldehyde as a reducing agent *Nano Lett.* **8** 2077–81

[58] Pejjai B, Minnam Reddy V R, Seku K, Pallavolu M R and Park C 2018 Eco-friendly synthesis of SnSe nanoparticles: effect of reducing agents on the reactivity of a Se-precursor and phase formation of SnSe NPs *New J. Chem.* **42** 4843–53

[59] Deignan G and Goldthorpe I A 2017 The dependence of silver nanowire stability on network composition and processing parameters *RSC Adv.* **7** 35590–7